Adsorption of cations at electrochemical interfaces revisited

Fabiola Domínguez-Flores[1] and Axel Groß[1]

[1]Institute of Theoretical Chemistry, Ulm University, 89081 Ulm, Germany

Abstract

At electrochemical interfaces, alkali-metal and alkaline-earth metal cations are usually described as solvated species that nonspecifically adsorb, whereas specifically adsorbed anions interact more directly with metal electrodes. However, the mode of cation-surface interaction remains poorly defined at the atomic scale because experiments typically measure averaged interfacial responses. Distinguishing hydration modulated polarization from localized ion-surface coupling therefore requires access to both the atomic structure and the redistribution of electronic charge. Using density functional theory molecular dynamics, we reexamine this distinction for hydrated K^+, Na^+, Ca^{2+}, oand Mg^{2+} at Pt(111), Au(111), and Ag(111) metal-water interfaces. Charge neutral, symmetric 3×3 cells containing one cation and five to seven water molecules at each interface allow for the study of compact, ion-rich layer configurations, rather than dilute electrolytes or electrodes maintained at an applied potential. Within the sampled compact layer configurations, structural sampling and charge density difference analysis indicate that cation adsorption spans a continuum of interfacial responses, ranging from diffuse, hydration modulated polarization to localized, compact layer coupling. Divalent cations exhibit the most persistent direct contact, and the selected divalent configurations show localized electronic redistribution, while monovalent cations are more sensitive to water coverage and substrate identity. Even predominantly non-contact cations can remain electronically relevant by polarizing the interfacial water layer and metal surface. These results suggest that cation adsorption within the compact interfacial region requires a local, structure dependent description that goes beyond simple specific or nonspecific classifications.

1 Introduction

Processes at electrochemical interfaces play an important role in electrochemical energy storage and conversion. In particular, ion hydration at solid-liquid interfaces is one of the key mechanisms that can shape the charge transfer kinetics in batteries and the activity-selectivity balance in electrocatalysis.[2–4] In interfacial electrochemistry, it is typically assumed that anions from the electrolyte adsorb specifically to the metal electrode, i.e., through direct chemical interactions,[5,6] which means that their solvation shell does not remain intact upon adsorption. In contrast, cations are generally assumed to adsorb nonspecifically, i.e., retaining their solvation shell upon adsorption.[4]

However, this traditional view has been increasingly reevaluated. In spite of their assumed nonspecific adsorption, the presence of cations at electrochemical interfaces has recently been found to play a crucial role in electrocatalytic processes. It has been shown that without metal cations in solution CO_2 electroreduction cannot proceed on copper, silver and gold electrodes, whereas mM solutions of Li^+, Na^+, K^+ or Cs^+ are sufficient to produce CO.[7,8] These findings indicate that cations are crucial for interfacial electrocatalytic processes. However, the exact mechanism by which cations promote these processes is still debated.[9,10] This shift in perspective is also evident in recent studies on alkaline hydrogen evolution[11,12] and in general frameworks for cation electrostatics at charged interfaces.[13,14] These developments suggest that cations should be regarded as active components of the compact interfacial environment, capable of modifying local electric fields, interfacial dipoles, and Helmholtz-layer properties, rather than merely as distant spectators that screen charge in the diffuse layer.

At the same time, it is fair to say that the atomistic nature of cation adsorption at metal-water interfaces is not fully understood. In bulk water, divalent cations generally exhibit stronger ion-water interactions, higher charge densities, and more rigid first hydration shells than monovalent cations. These differences are reflected in their greater hydration energies, stronger first shell ion-oxygen interactions, and more persistent hydration environments.[15–17] Monovalent cations, by contrast, tend to display more labile and weakly bound hydration environments, with hydration flexibility increasing from Na^+ to K^+ as ion-water interactions weaken.[15,18] Thus, Mg^{2+} and Ca^{2+} provide representative examples of strongly hydrated divalent cations, whereas Na^+ and K^+ allow a comparison to be made between monovalent cations of different sizes and with different degrees of hydration. However, it is not possible to transfer these bulk hydration trends directly to an electrochemical interface, where the local structure is determined by the simultaneous competition between ion-water, water-metal and ion-metal interactions.[19–21] This interfacial sensitivity is also supported by experimental evidence. In situ APXPS measurements have shown that the electrochemical double-layer potential drop and the potential of zero charge change as the applied potential and electrolyte concentration vary.[22] Consequently, distinguishing between specific and nonspecific adsorption becomes non-trivial. Depending on the identity of the ion, the substrate, and the local hydration environment, a cation may remain separated from the surface, undergo partial desolvation, or approach the surface closely enough to generate a localized interfacial response. On more reactive substrates such as Pt(111), the extent of this restructuring can depend on potential, local water structure, and surface state.[23,24]

In general, the atomistic elucidation of structures and processes at electrochemical interfaces represents a challenge. First of all, most experimental methods only provide integrated data with no local atomic resolution.[22,25,26] As far as atomistic simulations are concerned, the liquid nature of the electrolyte requires numerically demanding statistical averages.[27,28] Although molecular dynamics simulations based on classical interaction potentials can be used to make calculations for sufficiently large unit cells and time scales, standard non-polarizable models cannot accurately account for polarization and charge transfer effects.[15,18,29,30]

These questions are particularly relevant in electrocatalysis, where the structure of the compact layer can impact proton activity, charge screening, and electric field gradients at the interface. Changes in the organization of the hydration layer that depend on cations can influence proton-coupled electron transfer, double-layer charging and the activity and selectivity of electrochemical reactions.[31–33] This type of cation dependent restructuring is

also relevant beyond CO_2 reduction and alkaline hydrogen electrocatalysis. For example, alkali-metal cations can modify the Helmholtz-layer field and interfacial water orientation in oxygen reduction on Pt-based fuel cell electrodes.[33,34] Recent experimental and theoretical studies have also emphasized the importance of cation-induced restructuring of interfacial water and cation-dependent dipole formation at electrified interfaces.[22,35–37] Thus, a clearer atomistic description of how different cations interact with different metal surfaces is needed.

A reliable description of atomic structures and processes in interfacial electrochemistry often requires an explicit treatment of the electronic degrees of freedom, as provided by quantum chemical approaches such as density functional theory (DFT). Such methods can directly describe electronic charge redistribution, polarization, and charge transfer effects that are central to many electrochemical processes and are not captured explicitly by standard nonpolarizable force fields.[28,29,38–40] Here we present the results of systematic DFT-MD simulations of the interfacial solvation and adsorption of monovalent and divalent cations on Pt(111), Au(111), and Ag(111), spanning substantially different ion-surface interactions.

Our focus is on how the interplay of ion identity, charge density, hydration strength, water coverage, and substrate type determines the structure of interfaces and adsorption behavior. Specifically, we compare K^+, Na^+, and Ca^{2+} across all three metals, contrasting ions with different valencies, ionic sizes, and hydration strengths.[15–18] We also extend the Pt(111) series by including Mg^{2+} as an additional case, which helps to distinguish among the effects of ionic size, charge density, and hydration rigidity. This allows us to address the still poorly understood differences between mono- and divalent cations at electrochemical interfaces.[37,41,42] To limit the computational effort, we consider a (3×3) two-sided supercell with five to seven water molecules on each surface. These systems are not designed to replicate a bulk electrolyte, a long range diffuse layer, or the equilibrium pathway through which an ion approaches the electrode from the solution. Instead, they provide controlled, first principles models of ion-rich, compact layer environments, in which the identity of the ions, the metal substrate, and the local water loading can be systematically varied. Within this scope, the simulations allow us to examine how local water availability modifies cation coordination, ion-surface proximity, and the electronic response of the coupled ion-water-metal environment. Where appropriate, we also compare the solvated Na^+ and K^+ cases with the adsorption properties of the corresponding alkali metals at metal-vacuum interfaces.[43] This comparison is used only as a limiting structural reference for compact alkali-metal geometries in the absence of water.

We determine how ion identity, hydration environment, local water loading, and metal substrate jointly influence the structure and electronic response of cations sampling the compact interfacial region. Through the integration of hydration energetics, structural descriptors, sampled contact fractions, and charge density difference analysis, we can distinguish between localized compact layer coupling and more spatially displaced, hydration modulated interfacial polarization. This combined description illustrates why classifying cation adsorption as either specific or nonspecific does not capture the full range of local ion-water-metal configurations in these models.

2 Computational Methods

In this study we have carried out density functional theory molecular dynamics simulations (DFT-MD) using the Vienna Ab initio Simulation Package (VASP)[44,45] which is a reliable approach to address electrochemical systems from first principles.[46] We employed the RPBE functional[47] for electronic exchange-correlation complemented by D3(vdW-surf) dispersion corrections[48] that yield improved adsorption energetics on metal surfaces[49] and a proper description of the properties of liquid water.[50] Electron-core interactions were treated with the projector augmented-wave (PAW) method,[51] and a plane-wave kinetic energy cutoff of 400 eV was used after verifying the convergence of total energies. Self-consistent field (SCF) convergence was set to 10^{-5} eV using the RMM-DIIS algorithm with up to 1000 electronic iterations. The symmetric, two-sided setup minimizes artificial net dipoles. Meanwhile, dipole corrections along the surface normal were retained to reduce residual periodic image interactions arising from instantaneous asymmetries during MD.

DFT-MD simulations were performed in the canonical (NVT) ensemble at 298 K using a Langevin thermostat, a friction coefficient of 5 ps^{-1}, and a time step of 1 fs. Ion containing slab-water trajectories were equilibrated for 10 ps and then followed by 50-66 ps of production sampling. Reference simulations of bulk water and the pristine slab-water interface were sampled over shorter trajectories. Consistency over the analyzed intervals was assessed through block analysis[52] of mean energies, radial distribution functions (RDFs), and density profiles. Temporal block means and linear fits to $E_0(t)$ were used as descriptive diagnostics of stationarity over the analyzed production intervals. Block-to-block variations were propagated into the uncertainties of relative energy comparisons. Further details and representative analyses are provided in the Supplementary Information (SI).

Metal-water interfaces were modeled as 3×3 (111) slabs consisting of six atomic layers separated by approximately 15 Å of vacuum. Brillouin zone integration used a Γ-centered $1 \times 1 \times 1$ k-point mesh. The central two layers remained fixed at bulk lattice constants, while the outer four layers were fully relaxed by a pre-MD geometry optimization and fully mobile during the MD simulations. Cations (Na^+, K^+, Ca^{2+}, Mg^{2+}) were positioned at hcp-hollow sites on both slab surfaces and were not constrained during MD. This corresponds to a coverage of 1/9 ML per side. Each simulation cell was overall charge neutral, while the symmetric two-sided arrangement minimized artificial net dipole moments. The labels Na^+, K^+, Ca^{2+}, and Mg^{2+} denote the nominal oxidation states used to identify the ionic species. These labels do not indicate an integer charge localized on the cation in the combined system. The total electron count was the neutral stoichiometric count of the periodic cell, and no compensating background charge was introduced. Therefore, charge redistribution between the cation, water, and metal was allowed to develop self-consistently. For this reason, the formal quantity ze/A should be regarded as a formal charge equivalent areal density associated with one nominal ion per interface rather than as a calculated electrode charge density. Thus, we report the unambiguous structural loading of 1/9 ML per side, rather than assigning an electrode charge density to these charge neutral cells. Explicit solvation was modeled using $n = 5$, 6, or 7 H_2O molecules per side. These coverages were selected to sample different populations and coverage dependent arrangements of the first interfacial water layer. This analysis examines how local water availability influences ion coordination, ion-surface approach, and the hydration modulated electronic response of the metal. Since only the local

interfacial water population is explicitly represented, these cells do not reproduce the long range orientational polarization, dielectric screening, or bulk solvent response of an extended aqueous electrolyte. Therefore, the resulting structures and sampled contact fractions are interpreted as properties of the modeled compact layer configurations rather than equilibrium adsorption populations of ions exchanging with the bulk solution.

As an additional qualitative check the sensitivity to initial ion placement further, alternative trajectories were initialized with the cation above the interfacial water layer instead of next to the metal surface. The calculations included Pt-Mg^{2+}, Pt-Ca^{2+}, Pt-Na^{+}, and Pt-K^{+} with five and seven H_2O molecules per interface, as well as Au-Ca^{2+} and Ag-Ca^{2+} with seven H_2O molecules per interface. The trajectories were propagated for more than 20,000 MD steps. In all cases, the ions evolved toward more compact interfacial configurations. Notably, the divalent cations displaced or reorganized the initially intervening water molecules and reached short ion-metal separations that persisted over the subsequent trajectory. These results suggest that the compact configurations observed for the divalent ions are not solely inherited from an initially contacting geometry. More generally, the results demonstrate that the sampled near-surface configurations can be attained from significantly different initial ion positions. However, these calculations do not determine equilibrium adsorption free energies, establish unique equilibrium populations, or rule out additional metastable interfacial states.

Extended DFT-MD sampling of the pristine metal-water interface (slab + nH_2O, without ions) was restricted to Pt(111) and not performed for Au(111) and Ag(111). Mg^{2+} was also not considered for these two substrates due to the substantially higher computational cost associated with its slower solvation dynamics.

A bulk liquid-water reference simulation (33 H_2O, density $\sim$1 g cm^{-3}, 298 K, identical DFT settings, 1 fs time step) established the internal energy baseline. After 10 ps of equilibration, the 6.5 ps production trajectory was divided into three equal blocks. The block-to-block agreement supports the stability of the sampled local RDF features over the production interval, without implying convergence of slower dynamical or collective observables.

The per-molecule internal energy,

$$\mu^{U}_{\mathrm{H_2O,bulk}} = \frac{\langle U \rangle}{N} \tag{1}$$

was extracted from this trajectory, with the uncertainty estimated from 1 ps block averages.[52] This bulk reference is used solely to contextualize internal energy trends rather than free energies, in line with established best practices recognizing that complete thermodynamic descriptions require explicit entropic contributions from low-frequency vibrational modes.[36]

We used two complementary definitions to quantify the energy increase from adding successive water molecules to the symmetric slab-ion system. The first descriptor measures the internal energy change associated with a bulk-referenced hydration step, which involves adding two H_2O molecules per symmetric cell.

$$\Delta U^{(2\mathrm{H_2O})}_{\mathrm{step}}(N) = \langle E_0 \rangle_N - \langle E_0 \rangle_{N-1} - 2\mu^{U}_{\mathrm{H_2O,bulk}}, \quad \Delta U_{\mathrm{step}} = \frac{1}{2}\Delta U^{(2\mathrm{H_2O})}_{\mathrm{step}} \tag{2}$$

The second, applied exclusively to the Pt series for which slab only reference data were available, isolates the ion-specific contribution by subtracting the hydration profile of the pure slab + nH_2O system:

$$\Delta\Delta U_{\text{step}}^{\text{ion}}(N) = \frac{1}{2}\left([\langle E_0\rangle_{\text{slab+ion+}N} - \langle E_0\rangle_{\text{slab+ion+}N-1}] - [\langle E_0\rangle_{\text{slab+}N} - \langle E_0\rangle_{\text{slab+}N-1}]\right) \quad (3)$$

This difference quantifies the ion-induced change in the internal energy of water addition after subtracting the intrinsic water layering contribution of the pristine Pt(111)-water interface. Here N denotes the number of water molecules on each side of the symmetric slab, so the transition from $N-1$ to N corresponds to adding two water molecules to the full simulation cell, one at each interface. Therefore, the factor of 1/2 expresses the energy increment per added water molecule and per interface. Negative values of $\Delta\Delta U_{\text{step}}^{\text{ion}}$ indicate ion-induced stabilization relative to the pristine Pt(111)-water interface, while positive values indicate an ion-induced energetic penalty. All reported internal energies correspond to mean total energies $\langle E_0\rangle$ averaged over equilibrated DFT-MD trajectories. The resulting energetic increments (ΔU_{step} and $\Delta\Delta U_{\text{step}}^{\text{ion}}$) thus serve as internal energy descriptors of hydration and solvation at metal-water interfaces. They quantify relative stabilization trends among ions and hydration numbers while omitting entropic contributions, and capture only the energetic component of interfacial solvation thermodynamics.

The convergence of selected local structural descriptors was assessed using block analysis of radial distribution functions and density profiles, as detailed in the Supplementary Information (SI). For instance, the height of the first O-O RDF peak for Pt(111) exhibited a relative standard deviation of 4.4%, while the maximum of the oxygen z density in the first interfacial layer varied by 2.9% across the analyzed blocks. This limited variation among blocks supports the stability of these local structural features over the production interval.

Although our explicit water DFT-MD cells are relatively compact, they provide controlled reference systems in which ion identity, metal surface, and local water loading can be varied systematically. The fixed 3×3 two-sided slab with 5 to 7 H_2O molecules per side provides systematically comparable interfacial water loadings and sampled estimates of contact fractions, hydration numbers, and ion-metal distances within the present model system. A dedicated vacuum occupancy and connectivity analysis, reported in the SI, confirms that no water evaporates persistently or desorbs irreversibly in any system. Thus, all ions remain embedded in a contiguous interfacial water network. While this system size does not capture long range interfacial heterogeneity or the bulk solvent response, these compact models reveal local structural configurations associated with ion coordination and ion-surface proximity. This allows for consistent, coverage resolved comparisons between ions and metal substrates.

3 Results and Discussion

3.1 Energetic Landscape of Interfacial Hydration

Our objective is to quantify the internal energy contribution of interfacial hydration via the bulk referenced, per-water step energy ΔU_{step} (Eq. 2). Within this convention, positive ΔU_{step} indicates an internal energy penalty for transferring one water molecule from bulk liquid into the interfacial environment, whereas negative values indicate internal energy stabilization relative to bulk water. Since entropic contributions are not included,

we focus on internal energy trends and structural correlations rather than on absolute thermodynamic stability.

The analysis of ion specific contributions starts with Pt(111). The availability of pristine slab-water reference trajectories allows the ion induced contribution to be isolated through Eq. 3. For Au(111) and Ag(111), where such reference trajectories were not available, the comparison relies solely on the bulk-referenced step energy ΔU_{step}.

Figure 1 shows representative side view DFT-MD snapshots. These symmetric two-sided structures illustrate the sampled local hydration environments and provide structural references for the energetic and structural analysis below. Quantitative contact assignments are based on trajectory statistics rather than on individual snapshots.

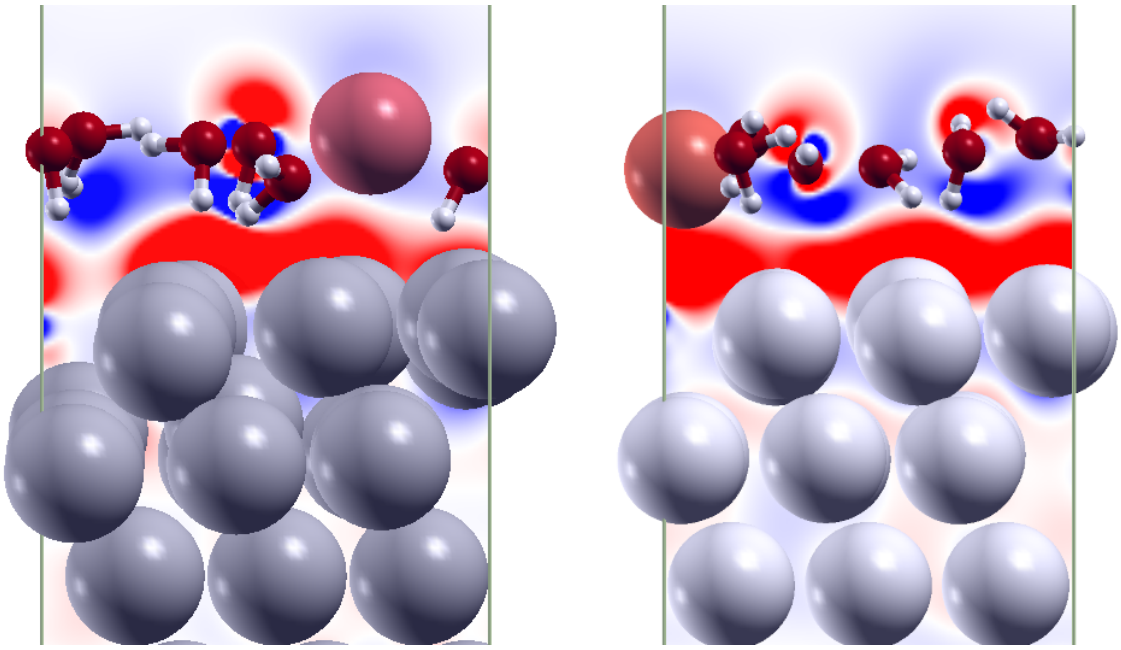


Figure 1: Representative side view DFT-MD snapshots of solvated Na^+ at Pt(111) and Ag(111) interfaces containing seven H_2O molecules per side. The snapshots illustrate the local arrangement of the ion, interfacial water molecules, and metal surface atoms in the sampled compact layer configurations.

3.1.1 Energetics on Pt(111)

For Pt(111), the presence of pristine slab-water reference trajectories allows the ion-induced contribution to water addition energetics to be evaluated through $\Delta\Delta U^{\text{ion}}_{\text{step}}(N)$ (Eq. 3). In this analysis, ΔU_{step} describes the overall referenced internal energy of water addition, whereas $\Delta\Delta U^{\text{ion}}_{\text{step}}$ measures the deviation from the corresponding pristine Pt(111)-water interface.

The resulting $\Delta\Delta U^{\text{ion}}_{\text{step}}(N)$ values reveal a two-step internal energy pattern on Pt(111) for the studied cations, with Ca^{2+} as the main exception. The first water addition step, from 5 to 6 H_2O molecules per side, is associated with a positive ion-induced internal energy increment. In contrast, the second step, from 6 to 7 H_2O molecules per side, is associated with ion induced stabilization (Fig. 2). The magnitude of both increments depends strongly on the cation. One possible interpretation is that the first step involves the disruption or reorganization of the interfacial water layer. The subsequent step then allows for a more cooperative rearrangement and ion-induced stabilization. However, this

interpretation is inferred from internal energy trends and does not constitute a direct analysis of structural basins, hydrogen bonds, or water orientation. The present analysis also does not quantify the accompanying entropic contribution.

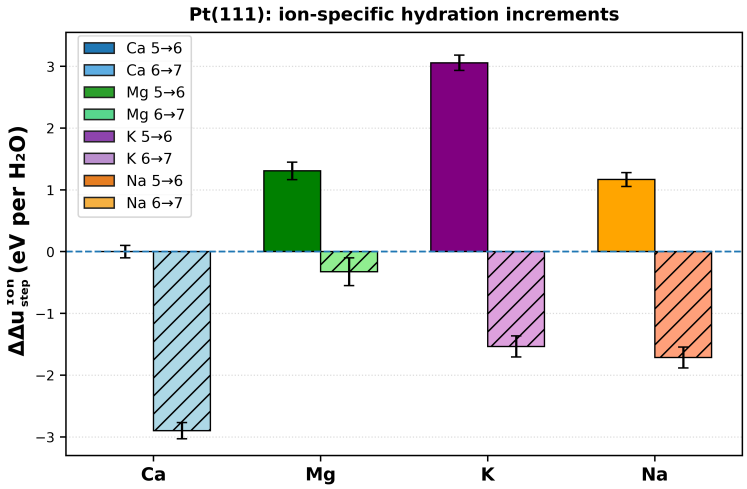


Figure 2: Ion-dependent internal energy increments for water addition on Pt(111), obtained by subtracting the corresponding pristine metal-water reference. Positive values indicate an ion-induced penalty to the hydrated slab, while negative values indicate ion-induced stabilization. Error bars indicate block-derived propagated uncertainties.

The magnitude of the first step ion induced penalty is strongly ion dependent. K^+ exhibits the largest positive increment, whereas Ca^{2+} remains close to neutral for the $5 \rightarrow 6$ H_2O step. These differences are consistent with the reorganization of the coupled ion-water-metal environment dependent on ions. However, the energy increments alone do not identify the microscopic balance between the ion-water stabilization and the restructuring of the Pt-water interface. For the $6 \rightarrow 7$ H_2O step, all cations show negative ion induced increments relative to the pristine Pt(111)-water baseline, indicating ion induced stabilization within this internal energy description. The magnitude of this stabilization varies among the ions, with Ca^{2+} showing the strongest stabilization, followed by Na^+ and K^+, while Mg^{2+} shows only a weak effect.

The bulk referenced increments in Fig. 3 show that the $5 \rightarrow 6$ water addition step is strongly uphill for K^+ and moderately uphill for Na^+ and Mg^{2+}, whereas Ca^{2+} remains close to neutral. The $6 \rightarrow 7$ step remains positive for K^+, Na^+, and especially Mg^{2+}, while Ca^{2+} again approaches neutrality. Thus, the ion-induced stabilization observed during the $6 \rightarrow 7$ step does not necessarily offset the internal energy cost of incorporating and reorganizing additional interfacial water.

Overall, Pt(111) lies in a competitive interfacial regime, where the stabilization and reorganization of the ordered Pt-water adlayer by ions and water have opposing energetic effects. The balance of these effects, which depends strongly on the identity of the ions, governs the energetics of water addition.

3.1.2 Metal Dependent Hydration Trends

The Pt(111) dataset shows that ion-specific contributions to the internal energy increments can be significant. For Au(111) and Ag(111), the combined metal-water and ion-water response is characterized by ΔU_{step}. Ion-specific decomposition is restricted

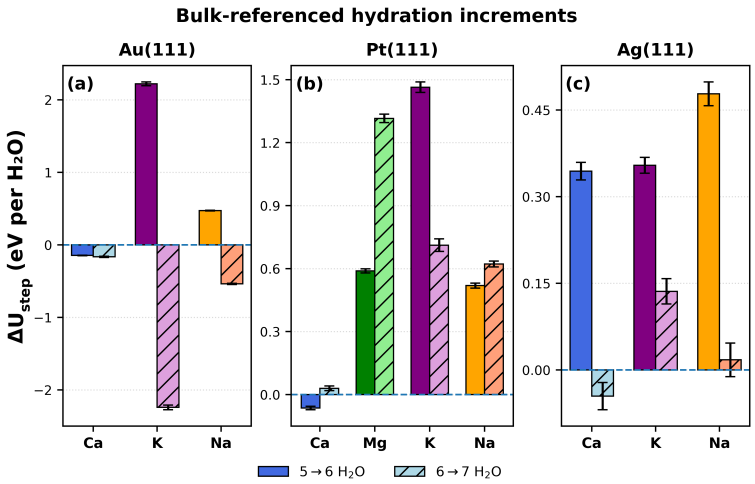


Figure 3: The internal energy cost of cation hydration on (Pt, Au, Ag)-(111), referenced to the bulk hydration step. Positive values indicate an internal energy penalty relative to bulk water, while negative values indicate stabilization. The sign and magnitude of increments depend on both ion identity and metal substrate.

to Pt(111), for which matched pristine interface trajectories are available. A comparison across metals (see Fig. 3) shows a substantial substrate dependence of the hydration energetics.

On Au(111), K^+ and Na^+ exhibit pronounced step-to-step compensation. The first water addition increments are unfavorable, whereas the increments of 6 to 7 H_2O are stabilizing. Ca^{2+} shows only minor increments for both steps. This pattern is consistent with a change in the coupled ion-water-metal response between the two hydration steps. However, the energy increments alone do not establish a specific disruption and reorganization mechanism.

On Ag(111), by contrast, the first water addition step is unfavorable for all three ions. The second step remains unfavorable for K^+, whereas the increments for Na^+ and Ca^{2+} are small and close to neutral within uncertainty. Overall, Ag(111) exhibits less complete energetic compensation than Au(111) when the sixth and seventh water molecules are added.

Pt(111) does not occupy a consistent intermediate position between Au(111) and Ag(111) with respect to the total increments. Rather, Pt(111) predominantly exhibits positive bulk-referenced increments for K^+, Na^+, and Mg^{2+}, while Ca^{2+} remains close to neutral. The Pt-only decomposition shows that a negative ion-induced contribution in the second step can coexist with a positive total ΔU_{step}. Thus, when expressed as $\Delta\Delta U^{\text{ion}}_{\text{step}}$, the Pt series retains the two-step energetic pattern described above, without assigning either step to a unique microscopic reorganization mechanism.

3.2 Charge density difference maps

We used charge density difference (CDD) maps to visualize the charge redistribution in real space associated with selected interfacial configurations. Direct contact was assigned independently of the CDD analysis, using the trajectory based geometric criteria, as defined in Section 3.3.1. The CDD analysis complements the contact statistics by providing information on electronic redistribution. However, it cannot independently determine whether a configuration is classified as contact or non-contact.

The charge density difference was calculated as:

$$\Delta\rho = \rho_{\text{slab+ion+water}} - \rho_{\text{slab}} - \rho_{\text{ion+water}}. \tag{4}$$

No net charge was added to or removed from the full system or fragment calculations used in this decomposition. Accordingly, $\rho_{\text{ion+water}}$ is the density of a neutral stoichiometric ion plus water fragment, used only as a reference fragmentation for defining Eq. 4; it is not the density of a pre-existing charged hydrated-ion fragment. The electron counts of the fragments were chosen so that the electron numbers of the slab and ion-plus-water references sum to the total electron number of the complete charge-neutral system. The same spin treatment as in the corresponding full system calculation was retained, with $\int \Delta\rho(\mathbf{r})\, d\mathbf{r} = 0$ by electron-number construction.

We evaluated all three charge densities using the same simulation cell, real-space grid, and at the same atomic positions as the complete system. This decomposition describes the electronic response generated by coupling the metal slab to the hydrated ion-water fragment. Therefore, it includes contributions from metal-water interactions and hydration modulated ion-surface coupling, and it should not be interpreted as a perturbation exclusive to the ion. Positive values of $\Delta\rho$, shown in blue, denote electron accumulation, while negative values, shown in red, denote electron depletion.

The maps correspond to snapshots extracted from the equilibrated portions of the $n = 7$ trajectories, thereby holding the interfacial water loading constant across the compared systems. The snapshots were selected based on structural criteria to illustrate well developed local hydration environments, without regard to the resulting CDD patterns. Each map represents an illustrative two-dimensional slice through a selected configuration rather than a trajectory average. The structural contact classification is defined independently of the CDD morphology, using the geometric criterion employed throughout the trajectory analysis.

3.2.1 Compact layer responses on Pt(111)

All four of the selected Pt(111) configurations shown in Fig. 4 exhibit a surface-normal redistribution at the metal-water interface. Electron depletion is concentrated near the uppermost Pt atoms, while electron accumulation develops outside the surface. The positions of nearby water molecules laterally modulate this interfacial electron accumulation region, indicating that the displayed response belongs to the coupled Pt-water-ion configuration rather than to a homogeneous displacement of charge at the metal surface.

In the selected Ca^{2+} and Mg^{2+} configurations shown, the ion-centered redistribution lies close to the compact layer response. For the Ca^{2+} configuration, the redistribution extends from the ion toward the nearby hydration waters and approaches the interfacial electron accumulation region above the Pt surface. In the displayed Mg^{2+} configuration, the ion is located slightly closer to the surface, compressing the surface-facing depletion region into the ion-surface gap. These maps are consistent with the short distance and high contact populations identified from the trajectory statistics. However, the statistical assignment comes from the geometric analysis rather than from the CDD slice itself.

The displayed Pt(111) configurations reveal that K^+ and Na^+ show a different spatial organization from the divalent cations. For both alkali cations, the ion-centered polarization feature can be distinguished from the interfacial electron accumulation region on the metal side. The positions of the surrounding oxygen atoms modulate the shape of the ion-centered lobes, indicating that the local response is largely associated with the

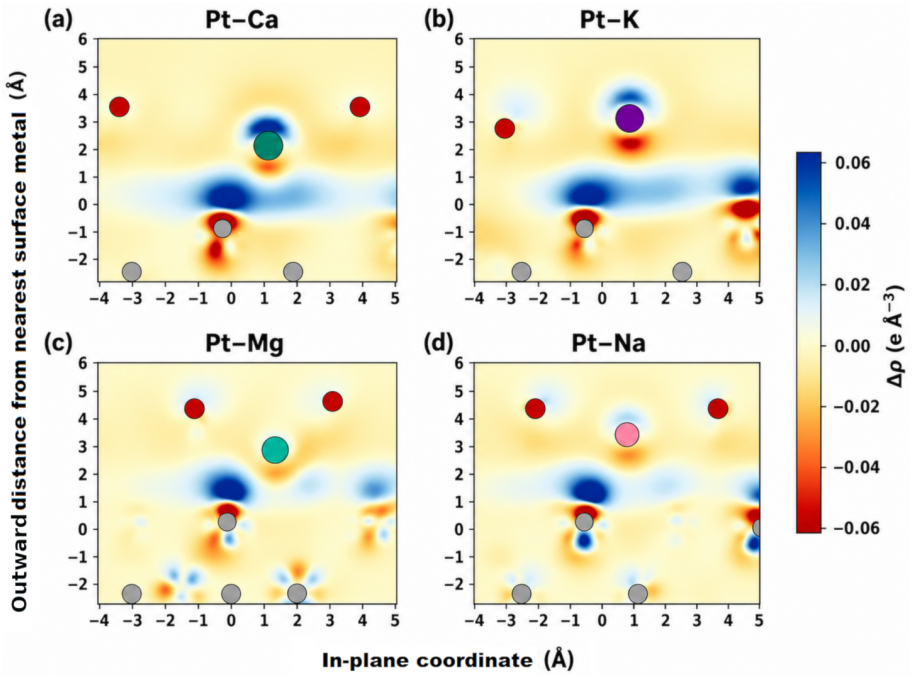


Figure 4: Two-dimensional charge density difference slices for selected hydrated ions at the Pt(111)-water interface: (a) Ca^{2+}, (b) K^+, (c) Mg^{2+}, and (d) Na^+. Blue indicates electron accumulation, and red indicates electron depletion, both over approximately $\pm 0.06\ e\text{Å}^{-3}$. Dark-red and gray markers denote water O and Pt atoms respectively. Larger markers identify Ca (green), K (purple), Mg (light green), and Na (pink). The axes show the in-plane position and the distance outward from the mean plane of the outermost metal layer.

polarization of the hydration environment. Thus, within the displayed slicing planes, the ion-centered and metal side features remain spatially separated, even though the metal-water interface exhibits a clear electronic response.

These selected Pt(111) slices illustrate that ion-centered and metal-side redistribution can be either closely associated or spatially separated. Geometric contact is not determined by either pattern, but rather by the trajectory based criterion.

3.2.2 Compact layer organization on Au(111) and Ag(111)

Figure 5 compares selected Au(111) and Ag(111) configurations using the same color scale. The selected Ag(111) slices show a more coherent electron accumulation at the interface outside the metal than the corresponding Au(111) slices. The Au(111) response is more fragmented and associated with nearby water molecules and surface sites. This comparison is morphological and configuration specific and should not be interpreted as an ensemble averaged difference in CDD amplitude.

The selected Na^+ slices show an intermediate spatial organization. The ion-centered response remains visible near the hydration environment, and the metal-side accumulation is shaped by the local arrangement of nearby water molecules and surface atoms. These selected $n = 7$ CDD slices provide the electronic context for Na^+ configurations on Au(111) and Ag(111). However, Na^+ coverage is determined by structural and contact statistics rather than by CDD maps alone.

The detailed CDD morphology of K^+ is substrate dependent. On Pt(111), the K-

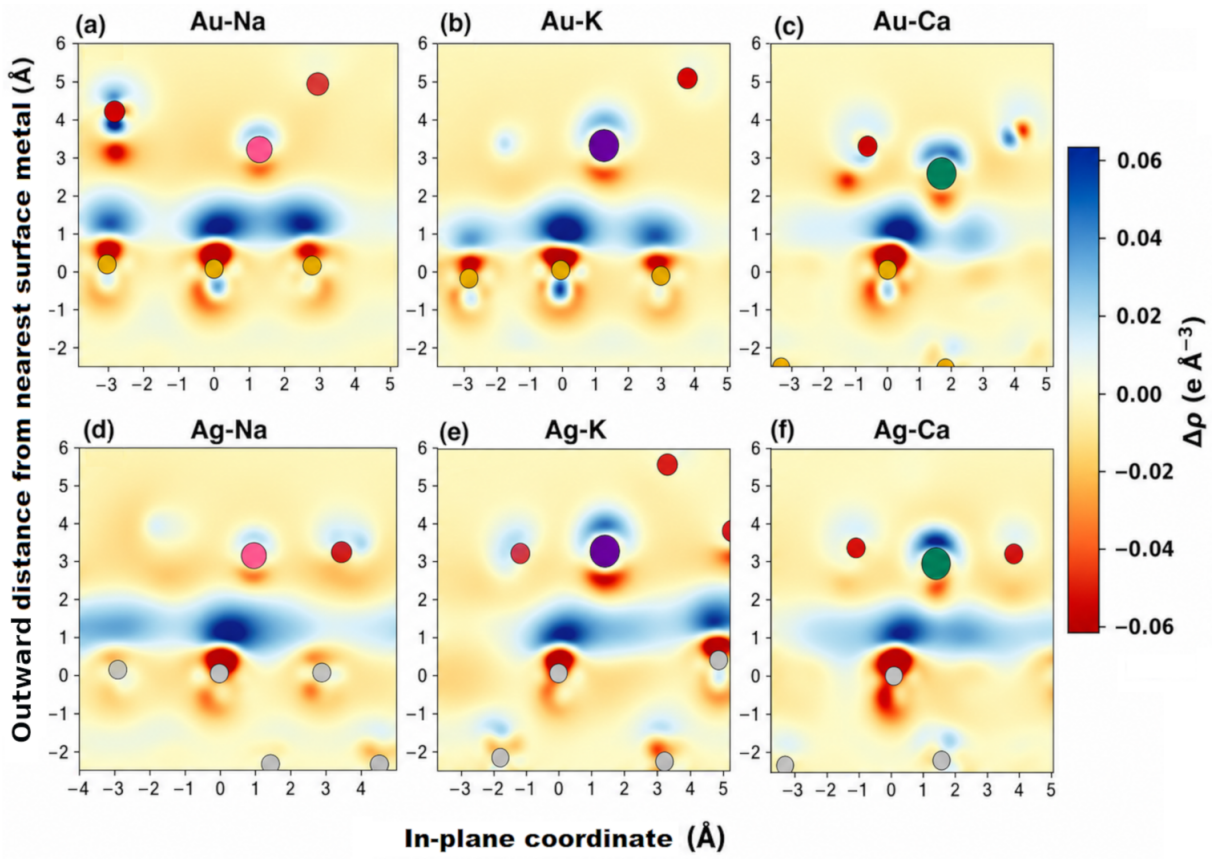


Figure 5: Two-dimensional charge density difference slices for selected hydrated Au(111) and Ag(111) systems: (a) Au-Na^+, (b) Au-K^+, (c) Au-Ca^{2+}, (d) Ag-Na^+, (e) Ag-K^+, and (f) Ag-Ca^{2+}. Blue and red regions indicate electron accumulation and depletion, respectively. Dark-red circular markers denote oxygen atoms from water molecules. Larger colored markers identify cations. Gold and gray markers denote Au and Ag atoms, respectively.

centered response is relatively diffuse and remains separated from the accumulation region near the surface. On Au(111), interfacial redistribution is more heterogeneous, modulated locally by surrounding water molecules and surface sites. The K-centered feature remains predominantly associated with the hydration environment. On Ag(111), the near-surface accumulation is broader and more laterally coherent. The displayed K^+ slice exhibits a pronounced dipolar feature normal to the surface around the ion. This ion-centered feature primarily overlaps with the hydration region rather than forming a continuous connection to the electronic response near the surface. Therefore, the pronounced K^+ dipolar feature observed in the Ag(111) configuration should not be interpreted as evidence of direct ion-metal contact.

For Ca^{2+}, the displayed Au(111) and Ag(111) configurations show a closer spatial relationship between the ion-centered redistribution and the compact layer. The Ca^{2+}-centered response extends toward the hydration shell and the interfacial electron accumulation region on the surface side. In the selected Ag-Ca^{2+} slice, the metal-side response is broader and more coherent laterally. In contrast, in the selected Au-Ca^{2+} slice, the response is more localized and strongly modulated by the nearby water arrangement.

Along with the trajectory based contact statistics, these selected CDD slices provide an electronic context for the structurally identified adsorption continuum. A comple-

mentary density of states (DOS) analysis is presented in Fig. S6. This analysis provides additional electronic structure context but is not considered an independent contact criterion. Here, "continuum" refers to graded variation across structural descriptors and the electronic response from the selected configurations. The CDD slices within the displayed planes illustrate configurations in which ion-centered redistribution is close to the compact layer response, as well as configurations in which the two features are spatially separated. However, the slices do not establish three-dimensional connectivity, quantify net charge transfer, predict capacitance, or determine the statistical prevalence of these patterns. Addressing these questions would require analyses beyond the scope of this study.

Therefore, even in a geometrically non-contact configuration, a cation can still be electronically relevant within the compact layer. By polarizing nearby water molecules, the cation can be associated with changes in the spatial organization of the interfacial electron accumulation region. This hydration modulated polarization may contribute to compact layer properties, including Helmholtz capacitance, as suggested by previous calculations. However, capacitance is not computed in the present work, and the CDD maps are interpreted as real-space, configuration-resolved evidence of local polarization in the selected configurations.[14,53]

3.3 Structural configurations from RDFs

We characterize the interfacial hydration environments using ion-oxygen and ion-metal radial distribution functions (RDFs). The resulting structural parameters for all metal surfaces, cations, and water coverages are compiled in Table 1. The ion-oxygen RDFs define the first shell cutoff at the first minimum, $r_{\mathrm{min}}^{\mathrm{ion-O}}$, from which hydration numbers are obtained (see Fig. 6). Divalent ions, Ca^{2+} and Mg^{2+}, show sharper first shell features and smaller ion-oxygen cutoffs than the monovalent ions, whereas Na^{+} and K^{+} display broader hydration distributions at larger ion-oxygen separations. The ion-metal distance distributions are used to identify the region of direct contact and near-surface residence. Because the interface is anisotropic, these structural descriptors are interpreted together with the operational direct contact criterion, which is summarized below and defined in detail in the Supplementary Information (SI). No single descriptor is considered evidence of specific or nonspecific adsorption.

3.3.1 Direct-Contact and Non-Contact Interfacial Configurations

A configuration was classified as direct contact if the following two conditions were met: (i) the nearest three-dimensional distance between the ion and the metal surface, $d_{\mathrm{ion-M}}$, was within the ion-specific direct contact cutoff and (ii) no oxygen atom from a water molecule was interposed between the ion and the same-side metal surface. The sampled contact fraction, $f_{\mathrm{cont}} = \langle \chi_{\mathrm{cont}} \rangle$, is the fraction of sampled ion configurations that satisfy both conditions. It is a finite trajectory structural descriptor rather than an equilibrium probability. The details of constructing the ion-specific cutoff, calculating the contact indicator and contact multiplicity, and counting hydration are provided in full in the SI.

In the vertical distribution analysis below, $d_{\mathrm{ion-surf}}$ denotes the displacement of the ion from the mean plane of the outermost same-side metal layer along the surface normal. This quantity differs from the three-dimensional ion-metal distance, $d_{\mathrm{ion-M}}$, used in the direct-contact criterion. No oxygen atoms from water molecules satisfied the interposition

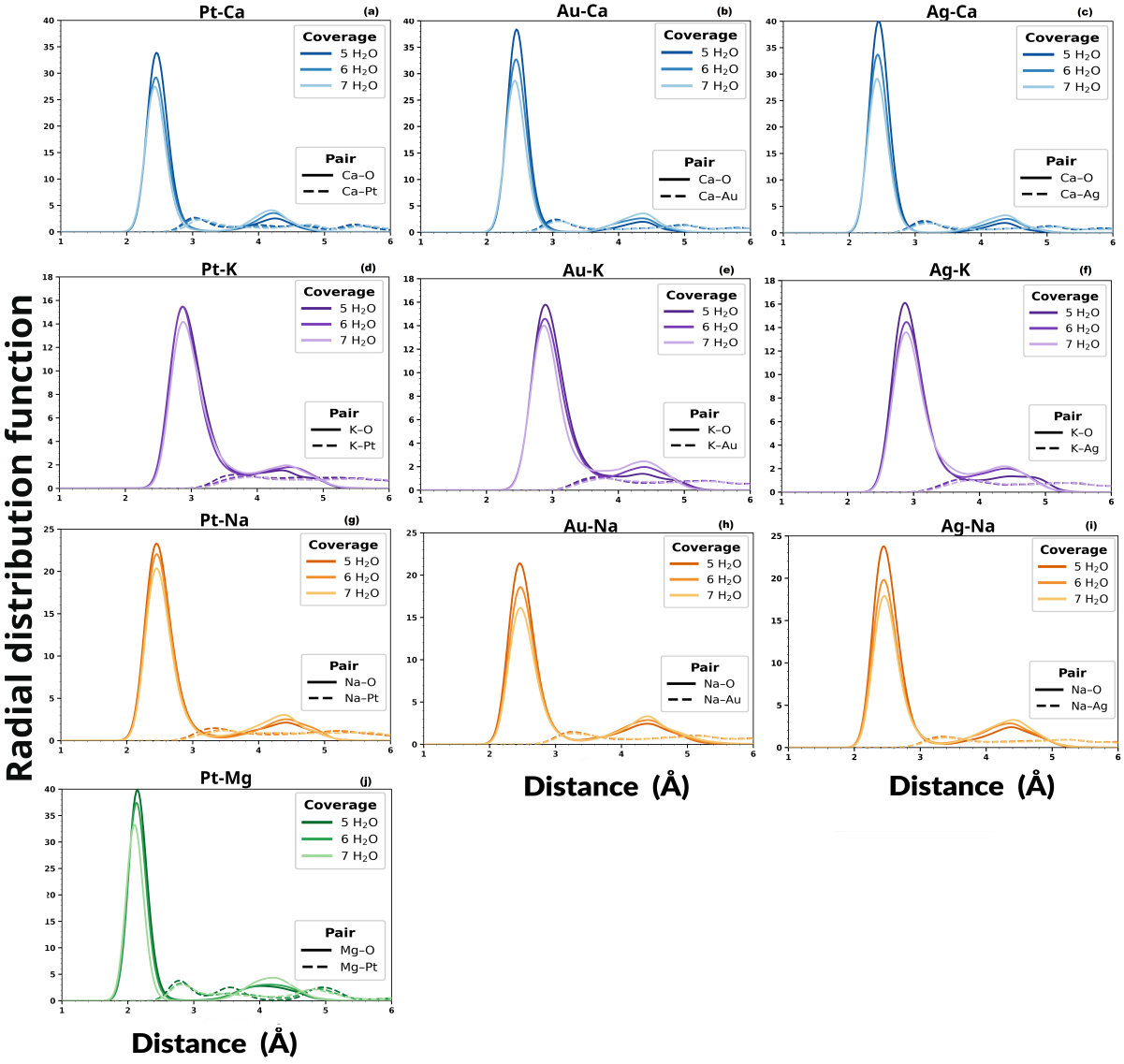


Figure 6: Radial distribution functions (RDFs) for ion-O (solid) and ion-metal (dashed). Panels show Ca^{2+} (a-c), K^+ (d-f), Na^+ (g-i) and Mg^{2+} (j) on Pt(111), Au(111), and Ag(111) surfaces for coverages of 5, 6, and 7 H_2O per interface (shades from darker to lighter).

criterion in the analyzed frames. Consequently, configurations classified as non-contact correspond to samples with $d_{\mathrm{ion-M}} > r_{\mathrm{c},i}^{\mathrm{ion-M}}$, rather than to water separated configurations. Water separated configurations remain part of the general geometric definition, but this category was not observed in the sampled trajectories.

The analysis of ion hydration was conducted independently of the contact classification. The cutoff for the first hydration shell, $r_{\mathrm{min}}^{\mathrm{ion-O}}$, was defined as the first minimum of the ion-oxygen radial distribution function on the same side. For each ion sample, the hydration number was defined as the number of oxygen atoms from water within this cutoff on the same side. The most probable value of this instantaneous coordination number is denoted by n_1, whereas

$$N_{\mathrm{hyd}} = \left\langle N_{\mathrm{O}} \left(r \leq r_{\mathrm{min}}^{\mathrm{ion-O}} \right) \right\rangle$$

is the corresponding trajectory averaged hydration number.

According to the vacuum-occupancy and connectivity analysis reported in the SI, no persistent detached water population was evident within the simulated time windows. Therefore, changes in the sampled contact fraction, contact multiplicity, and hydration are interpreted as reorganizations within the retained interfacial water layer rather than consequences of systematic water loss from the simulation cell.

3.3.2 Ion-Specific Hydration and Contact-like Adsorption

The divalent ions maintained near-continuous contact throughout the trajectories. On Pt(111), the mean vertical distance of Mg^{2+} from the outermost Pt layer remains at 1.917-2.002 Å across the three water coverages and has $f_{\mathrm{cont}} = 0.998$-$1.000$. The most probable hydration number is $n_1 = 3$, and the mean hydration number is $N_{\mathrm{hyd}} = 2.872$-3.147. This indicates that approximately three oxygen atoms from water molecules remain in the first hydration shell and that the metal surface participates in the local coordination environment. Conditional contact coordination decreases from $\langle N_M^{\mathrm{cont}} \rangle = 2.368$ at $n = 5$ to 2.028 at $n = 7$. Thus, Mg^{2+} remains in persistent contact with Pt(111) over the sampled trajectories, but the number of Pt atoms defining its local contact site decreases slightly as the water coverage increases.

In a similar manner, Ca^{2+} remains predominantly in contact with all three metal surfaces throughout the sampled trajectories. Its sampled contact fraction ranges from 0.991 to 0.999, and $n_1 = 4$ for all systems and water coverages. On Pt(111), N_{hyd} increases from 3.598 to 3.938 as n increases from 5 to 7. This is accompanied by an increase in $d_{\mathrm{ion-surf}}$ from 2.364 to 2.562 Å and a decrease in $\langle N_M^{\mathrm{cont}} \rangle$ from 2.130 to 1.983. Similar trends occur on Au(111) and Ag(111). Direct contact remains the predominant sampled state, but its average hydration increases and the number of metal atoms in the local contact environment decreases modestly as water coverage increases. The mean ion surface distance follows the order $d_{\mathrm{ion-surf}}(\mathrm{Pt}) < d_{\mathrm{ion-surf}}(\mathrm{Au}) < d_{\mathrm{ion-surf}}(\mathrm{Ag})$ for Ca^{2+} at each coverage. These results demonstrate that increased hydration does not necessarily eliminate direct contact. Rather, hydration and surface coordination adjust simultaneously.

Monovalent ions have substantially lower sampled contact fractions that are more coverage dependent. Among the studied ions on every surface, K^+ has the lowest f_{cont}. On Pt(111), f_{cont} decreases from 0.55 at $n = 5$ to 0.33 and 0.30 at $n = 6$ and 7, respectively. This decrease is accompanied by increases in $d_{\mathrm{ion-surf}}$ from 3.104 to 3.476 Å and in N_{hyd} from 3.774 to 4.782. The most probable hydration number increases correspondingly from $n_1 = 4$ to $n_1 = 5$ at the highest coverage. When contact does occur, K^+ interacts with only approximately one surface atom: $\langle N_M^{\mathrm{cont}} \rangle = 1.266$-$1.367$ on Pt(111). Therefore, K^+ remains an interfacial ion. However, its increasing hydration and ion-surface separation favor more vertically displaced non-contact configurations as the amount of interfacial water increases.

The same qualitative behavior is observed for K^+ on Au(111) and Ag(111). As the water coverage increases from 5 to 7 molecules per interface, the sampled contact fraction decreases from 0.48 to 0.34 on Au and from 0.44 to 0.31 on Ag. The ordering among the three metals is not constant with coverage. Pt has the largest K^+ sampled contact fraction at $n = 5$, Ag has the largest value at $n = 6$, and Au gives the largest value at $n = 7$. Thus, the differences among the metals are smaller and less systematic than the overall decrease with increasing water coverage. The dominant structural trend for K^+ is the progressive population of more highly hydrated, vertically displaced non-contact

Table 1: Sampled ion-surface contact fractions, hydration descriptors, and surface-normal distances for hydrated cations at Pt(111), Au(111), and Ag(111) interfaces.

System	n (H_2O)	n_1	f_{cont}	$\langle N_M^{cont} \rangle$	r_{min}^{ion-O} / Å	$d_{ion-surf}$ / Å	N_{hyd}
Pt(111)							
PtMg	5	3	1.00	2.368	2.930	1.917	2.872
	6	3	1.00	2.162	2.950	2.002	3.147
	7	3	1.00	2.028	2.950	1.967	3.000
PtCa	5	4	1.00	2.130	3.310	2.364	3.598
	6	4	1.00	2.058	3.310	2.513	3.749
	7	4	1.00	1.983	3.250	2.562	3.938
PtNa	5	3	0.72	1.465	3.390	2.811	3.206
	6	4	0.46	1.394	3.390	2.997	3.587
	7	4	0.51	1.312	3.290	3.011	3.829
PtK	5	4	0.55	1.367	3.890	3.104	3.774
	6	4	0.33	1.266	3.850	3.403	4.187
	7	5	0.30	1.279	3.850	3.476	4.782
Au(111)							
AuCa	5	4	1.00	1.964	3.250	2.518	3.869
	6	4	1.00	1.826	3.250	2.587	3.984
	7	4	1.00	1.788	3.290	2.640	4.008
AuNa	5	3	0.84	1.457	3.350	2.908	2.921
	6	3	0.77	1.487	3.370	2.955	3.120
	7	3	0.74	1.420	3.370	2.973	3.214
AuK	5	4	0.48	1.436	3.890	3.295	3.847
	6	4	0.37	1.431	3.830	3.382	4.193
	7	4	0.34	1.341	3.670	3.414	4.284
Ag(111)							
AgCa	5	4	1.00	1.967	3.350	2.597	3.978
	6	4	1.00	1.843	3.230	2.663	4.004
	7	4	0.99	1.708	3.250	2.709	4.119
AgNa	5	3	0.69	1.342	3.390	2.991	3.096
	6	3	0.63	1.348	3.310	3.025	3.162
	7	3	0.57	1.332	3.310	3.103	3.329
AgK	5	4	0.44	1.256	3.870	3.342	3.670
	6	4	0.39	1.333	3.770	3.388	4.042
	7	5	0.31	1.266	3.830	3.468	4.663

Parameter	Description
System	Metal-ion pair analyzed at the stated metal surface.
n (H_2O)	Number of water molecules per interface. The symmetric cell contains $2n$ water molecules.
n_1	Most probable number of same-side oxygen atoms from water molecules within r_{min}^{ion-O}.
f_{cont}	Fraction of analyzed configurations that satisfy the ion-metal distance and water interposition criteria. It is a finite-trajectory descriptor, not an equilibrium probability.
$\langle N_M^{cont} \rangle$	Conditional mean number of contacted same-side surface-metal atoms, evaluated only when direct contact is present.
r_{min}^{ion-O}	First minimum of the ion-O RDF, used as the hydration cutoff.
$d_{ion-surf}$	Mean surface-normal distance from the ion to the outermost same side metal plane.
N_{hyd}	Mean number of same-side oxygen atoms from water molecules within r_{min}^{ion-O}.

configurations.

Na^+ exhibits intermediate behavior between the persistently contacting divalent ions and the more weakly contacting K^+. On Pt(111), f_{cont} decreases from 0.72 at $n = 5$ to 0.46 at $n = 6$, and then shows a modest apparent recovery to 0.51 at $n = 7$. This apparent non-monotonic response is accompanied by a progressive increase in hydration. Specifically, n_1 changes from 3 to 4 and N_{hyd} increases from 3.206 to 3.829. The mean ion-surface distance also increases from 2.811 to 3.011 Å. The modest apparent recovery of contact at $n = 7$ does not correspond to dehydration. Rather, the trajectory contains a slightly larger sampled fraction of direct contact configurations at $n = 7$ despite maintaining high average first-shell hydration. Since these fractions are derived from individual finite trajectories and lack an uncertainty estimate based on independent trajectories, the slight difference between $n = 6$ and $n = 7$ is treated descriptively rather than as evidence of a statistically significant reentrant trend.

The metal dependence is clearer for Na^+ than for K^+. Au(111) consistently yields the highest Na^+ sampled contact fraction, with $f_{cont} = 0.84$, 0.77, and 0.74 for $n = 5$, 6 and 7, respectively. The corresponding values on Ag(111) are 0.69, 0.63, and 0.57, and on Pt(111), they are 0.72, 0.46, and 0.51. Thus, Na^+ retains a substantial contact population on Au even as its hydration increases. However, contact is more strongly reduced at intermediate and high coverage on Pt and Ag.

Overall, the sampled contact statistics reveal an ion-dependent structural continuum. This continuum ranges from nearly continuous contact of Mg^{2+} and Ca^{2+}, to the intermediate behavior of Na^+, to the larger fractions of vertically displaced non-contact configurations sampled by K^+. Position within this continuum depends on both metal identity and water coverage, rather than on a simple dichotomy between specific and nonspecific adsorption.

3.3.3 Metal-surface effects

No universal substrate hierarchy was observed in the sampled contact fractions. The substrate dependence is ion-specific. The divalent ions remain predominantly or nearly continuously contacting within the systems studied, whereas the monovalent ions respond more strongly to both metal identity and water coverage.

For K^+, increasing water coverage decreases f_{cont} on all three metals. However, the coverage interval with the greatest decrease depends on the substrate. It occurs from 5 to 6 H_2O on Pt(111) and Au(111), and from 6 to 7 H_2O on Ag(111). For Na^+, Au(111) and Ag(111) show monotonic decreases. However, Pt(111) shows a modest sampled increase from $n = 6$ to $n = 7$. Without an independent uncertainty estimate, the nonmonotonicity specific to Pt is interpreted descriptively rather than as a statistically established transition.

One plausible explanation for the energetic trends is that different substrates alter the compact ion-water-metal configurations sampled within the trajectories, as well as the response of the interfacial water layer. Although complementary RDF and DOS analyses are reported in the Supplementary Information (SI), they do not uniquely identify the microscopic reorganization mechanism.

3.3.4 Surface-normal ion-height distributions

We characterized the vertical component of the adsorption dynamics from the full distributions of the instantaneous surface-normal ion height, $d_{ion-surf}$ (Fig. 7); the correspond-

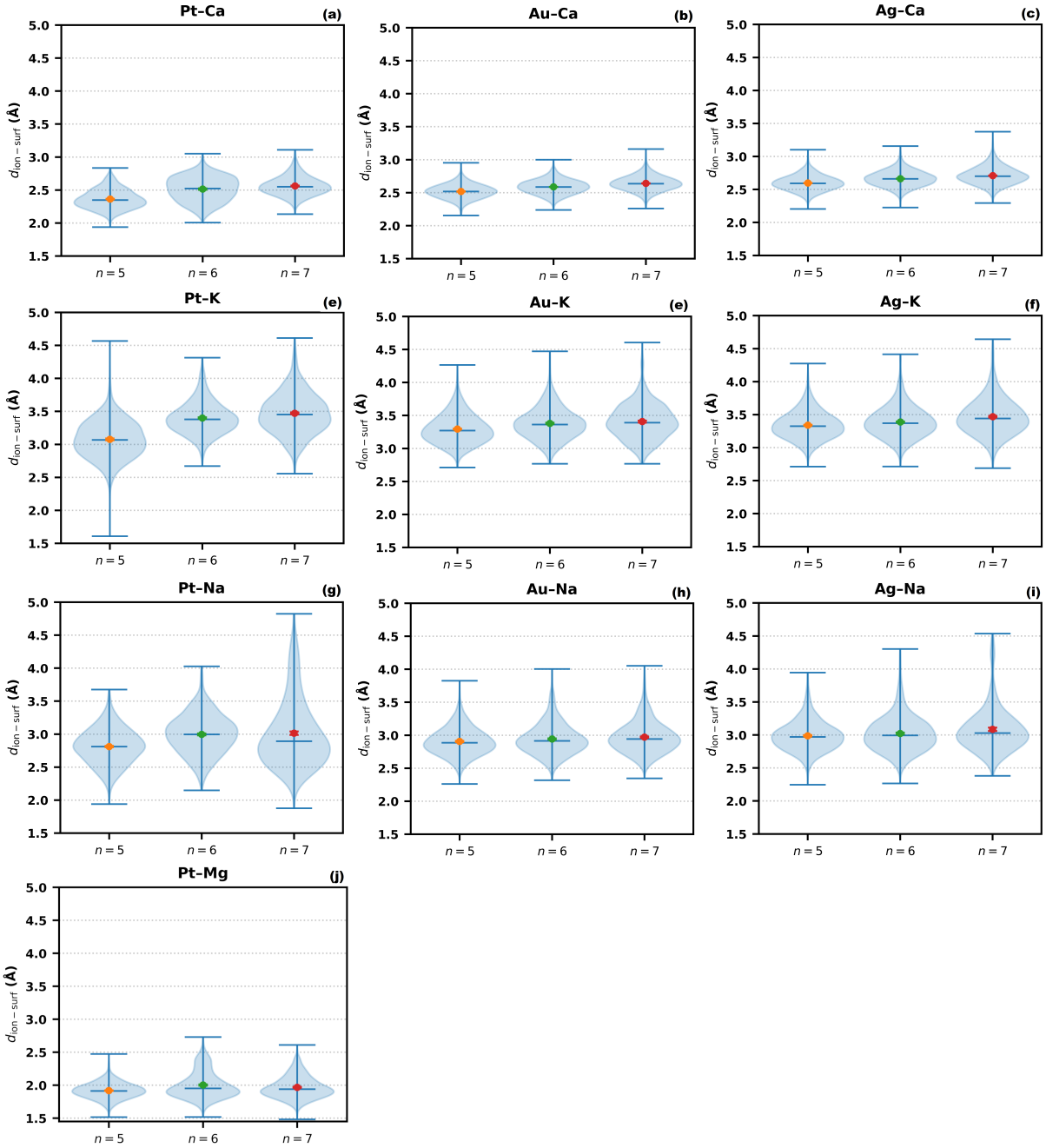


Figure 7: Distributions of the instantaneous surface-normal ion height, $d_{\mathrm{ion-surf}}$, for hydrated cations are shown for the investigated metal-water interfaces. Each violin plot shows the distribution obtained with five, six, or seven water molecules per interface. Within each panel, violin widths are normalized independently to represent the shape of the sampled density and are not quantitatively comparable among panels. The central horizontal line denotes the median, the marker denotes the mean, and the whiskers indicate the sampled range. Mg^{2+} was not simulated on Au(111) or Ag(111). The vertical-axis limits differ among ion groups to show the relevant height ranges.

ing nearest three-dimensional ion-metal distance distributions are reported in Fig. S7. These distributions provide additional information beyond the mean values in Table 1, particularly regarding their widths, asymmetry, long-distance tails, and the coexistence of compact and vertically displaced configurations.

The divalent ions show the narrowest and most strongly surface-localized distributions. Mg^{2+} on Pt(111) remains concentrated at short heights across all three coverages. Ca^{2+} is also localized on all three metals, but its distribution shifts outward from Pt to Au to Ag, developing somewhat broader upper tails on Ag(111). Na^{+} is more heterogeneous: the Pt(111) $n = 7$ distribution develops a pronounced long-distance tail approaching 5 Å, demonstrating that a modest sampled recovery in f_{cont} can coexist with a broad population of vertically displaced configurations. The Au-Na^{+} distribution remains comparatively compact, whereas the Ag-Na^{+} distribution broadens toward higher $d_{\mathrm{ion-surf}}$ as hydration increases.

K^{+} has the broadest height distributions and the most prominent coexistence of compact, near-surface configurations and more vertically displaced ones. The Pt-K^{+} distribution changes most strongly between five and six H_2O, while the Ag-K^{+} $n = 7$ case shows one of the longest upper tails. These distributional features reinforce the conclusion that a single mean height is insufficient to characterize the sampled interfacial state.

As a dry adatom reference, vacuum DFT calculations for neutral sodium (Na) and potassium (K) on Pt(111) report adatom-surface distances of 2.41 and 2.82 Å, respectively.[43] These values are only about 0.4-0.5 Å smaller than the corresponding mean distances plotted in Fig. 7, and the smallest Pt-Na and Pt-K distances found in the AIMD simulations are even smaller than the vacuum results. This indicates that the solvated ions can sample short ion-metal distances with the metal electrodes, but it does not by itself establish persistent direct contact.

Overall, the violin plot distributions complement f_{cont} by resolving the breadth, asymmetry, tails, and coexistence of compact and displaced populations sampled within each trajectory.

4 Conclusions

Using explicit water DFT-MD simulations, we studied how ion identity, metal substrate, and local water coverage influence cation configurations at Pt(111), Au(111), and Ag(111). These compact layer models capture the electronic response of the metal, the immediate hydration of the ions, and the reorganization of interfacial water at finite temperature, enabling systematic comparisons within the sampled interfacial region. We combine energetic, structural, contact, and charge density difference (CDD) descriptors to differentiate geometric contact from the electronic response of the metal-water interface.

Ion identity provides the clearest structural contrast. Throughout the sampled trajectories on all three metals, Ca^{2+} remains predominantly in contact ($f_{\mathrm{cont}} > 0.99$), while Mg^{2+} remains in near-continuous contact with Pt(111). Both ions are vertically localized, with Ca^{2+} lying farther from the surface and showing broader distributions on Ag(111). Increasing water coverage suppresses K^{+} contact with all three metals. However, the magnitude of this decrease and the surface-normal distributions remain metal-dependent. Na^{+} samples mixed contact and non-contact configurations and exhibits an apparent non-monotonic response on Pt(111). Contact increases modestly at seven water molecules, despite a broad surface-normal distribution with an extended upper tail. Thus, the change in the Pt-Na^{+} interaction is described as only a modest apparent recovery in the sampled trajectory rather than as a statistically established reentrant transition. No universal substrate hierarchy emerges. Rather, each metal modifies the accessibility of short range configurations in an ion-specific manner. Additional water molecules alter the balance

of contact and non-contact configurations in a substrate- and ion-dependent manner. Thus, the sampled contact fraction and surface-normal distance provide complementary descriptions of the interfacial structure.

CDD analysis provides electronic context for the structural trends observed in the selected $n = 7$ configurations. The displayed Ca^{2+} and Mg^{2+} configurations show localized ion-centered redistribution close to the compact layer response, consistent with strong local ion-surface coupling. K^+ shows greater spatial separation between the ion-centered and metal-side features, with the local electronic response strongly modulated by its hydration environment. Within the present compact layer models, cation behavior is therefore better described as a continuum ranging from persistent contact with localized ion-surface coupling to more spatially displaced, hydration modulated interfacial polarization. Notably, a geometrically non-contact cation can remain electronically relevant without requiring a water molecule to be interposed between the ion and the surface.

References

[1]

[2] Conway, B. E. *Electrochemical Supercapacitors: Scientific Fundamentals and Technological Applications;* Springer US: Boston, MA, 1999.

[3] Bard, A. J.; Faulkner, L. R. *Electrochemical Methods: Fundamentals and Applications;* John Wiley & Sons: , 2 ed.; 2001.

[4] Schmickler, W.; Santos, E. *Interfacial Electrochemistry;* Springer: Berlin, Germany, 2 ed.; 2010.

[5] Gossenberger, F.; Roman, T.; Groß, A. *Electrochim. Acta* **2016,** *216,* 152 - 159.

[6] Gossenberger, F.; Juarez, F.; Groß, A. *Front. Chem.* **2020,** *8,* 634.

[7] Monteiro, M.; Dattila, F.; Hagedoorn, B.; Garcia-Muelas, R.; Lopez, N.; Koper, M. *Nat. Catal.* **2021,** *4,* 654.

[8] Monteiro, M. C. O.; Dattila, F.; López, N.; Koper, M. T. M. *J. Am. Chem. Soc.* **2022,** *144,* 1589-1602.

[9] Le, D.; Rahman, T. S. *Nat. Catal.* **2022,** *5,* 977.

[10] Qin, X.; Hansen, H. A.; Honkala, K.; Melander, M. M. *Nat. Comm.* **2023,** *14,* 7607.

[11] Ringe, S. *Current Opinion in Electrochemistry* **2023,** *39,* 101268.

[12] Xu, P.; Wang, R.; Zhang, H.; Carnevale, V.; Borguet, E.; Suntivich, J. *J. Am. Chem. Soc.* **2024,** *146,* 2426–2434.

[13] Resasco, J. *JACS Au* **2025,** *5,* 5253–5266.

[14] Domínguez-Flores, F.; Groß, A.; Schmickler, W. *J. Phys. Chem. C* **2026,** *130,* 2475–2481.

[15] Biriukov, D.; Wang, H.-W.; Rampal, N.; Tempra, C.; Kula, P.; Neuefeind, J. C.; Stack, A. G.; Předota, M. *J. Chem. Phys.* **2022,** *156,* 194505.

[16] Liu, J.; Liu, R.; Cao, Y.; Chen, M. *Phys. Chem. Chem. Phys.* **2023,** *25,* 983–993.

[17] Santos, E. *Electrochim. Acta* **2024,** *497,* 144532.

[18] Kiyohara, K.; Minami, R. *J. Chem. Phys.* **2018,** *149,* 014705.

[19] Ito, M.; Nakamura, M. *Faraday Discuss.* **2002,** *121,* 71–84.

[20] Otani, M.; Sugino, O. *Phys. Rev. B* **2006,** *73,* 115407.

[21] Melander, M. M.; Kuisma, M. J.; Christensen, T. E. K.; Honkala, K. *J. Chem. Phys.* **2018,** *150,* 041706.

[22] Favaro, M.; Jeong, B.; Ross, P. N.; Yano, J.; Hussain, Z.; Liu, Z.; Crumlin, E. J. *Nat. Comm.* **2016,** *7,*.

[23] Sakong, S.; Groß, A. *J. Chem. Phys.* **2018,** *149,* 084705.

[24] Le, J.-B.; Chen, A.; Li, L.; Xiong, J.-F.; Lan, J.; Liu, Y.-P.; Iannuzzi, M.; Cheng, J. *JACS Au* **2021,** *1,* 569-577.

[25] Garlyyev, B.; Xue, S.; Watzele, S.; Scieszka, D.; Bandarenka, A. S. *J. Phys. Chem. Lett.* **2018,** *9,* 1927-1930.

[26] Wu, J. *Chem. Rev.* **2022,** *122,* 10821-10859.

[27] Groß, A.; Sakong, S. *Curr. Opin. Electrochem.* **2019,** *14,* 1 - 6.

[28] Groß, A. *Curr. Opin. Electrochem.* **2023,** *40,* 101345.

[29] Groß, A.; Sakong, S. *Chem. Rev.* **2022,** *122,* 10746-10776.

[30] Darby, M. T.; Cucinotta, C. S. *Curr. Opin. Electrochem.* **2022,** *36,* 101118.

[31] Hammes-Schiffer, S. *Chem. Rev.* **2010,** *110,* 6937-6938 PMID: 21141827.

[32] Ledezma-Yanez, I.; Wallace, W. D. Z.; Sebastián-Pascual, P.; Climent, V.; Feliu, J. M.; Koper, M. T. M. *Nature Energy* **2017,** *2,* 17031.

[33] Kelly, S. R.; Kirk, C.; Chan, K.; Nørskov, J. K. *J. Phys. Chem. C* **2020,** *124,* 14581-14591.

[34] Marković, N. M.; Schmidt, T. J.; Stamenković, V.; Ross, P. N. *Fuel Cells* **2001,** *1,* 105-116.

[35] Sakong, S.; Forster-Tonigold, K.; Groß, A. *J. Chem. Phys.* **2016,** *144,* 194701.

[36] Domínguez-Flores, F.; Kiljunen, T.; Groß, A.; Sakong, S.; Melander, M. M. *J. Chem. Phys.* **2024,** *161,* 044705.

[37] Alves Nogueira, J.; Dias Germano, L.; Domenico De Angelis, L.; Córdoba de Torresi, S. I. *Curr. Opin. Electrochem.* **2025,** *52,* 101701.

[38] Surendralal, S.; Todorova, M.; Neugebauer, J. *Phys. Rev. Lett.* **2021,** *126,* 166802.

[39] Li, X.-Y.; Chen, A.; Yang, X.-H.; Zhu, J.-X.; Le, J.-B.; Cheng, J. *J. Phys. Chem. Lett.* **2021,** *12,* 7299-7304.

[40] Li, L.; Eggert, T.; Reuter, K.; Hörmann, N. G. *J. Am. Chem. Soc.* **2025,** *147,* 22778-22784.

[41] Montenegro, A.; Dutta, C.; Mammetkuliev, M.; Shi, H.; Hou, B.; Bhattacharyya, D.; Zhao, B.; Cronin, S. B.; Benderskii, A. V. *Nature* **2021,** *594,* 62–65.

[42] Trasatti, S. *J. Electroanal. Chem. Interfacial Electrochem.* **1972,** *39,* 163-184.

[43] Koverga, A. A.; Ticianelli, E. A.; Groß, A. *Appl. Surf. Sci.* **2026,** *718,* 164918.

[44] Kresse, G.; Furthmüller, J. *Comp. Mater. Sci.* **1996,** *6,* 15-50.

[45] Kresse, G.; Furthmüller, J. *Phys. Rev. B* **1996,** *54,* 11169–11186.

[46] Euchner, H.; Groß, A. *Physical Review Materials* **2022,** *6,* 040302.

[47] Hammer, B.; Hansen, L. B.; Nørskov, J. K. *Phys. Rev. B* **1999,** *59,* 7413–7421.

[48] Grimme, S.; Antony, J.; Ehrlich, S.; Krieg, H. *J. Chem. Phys.* **2010,** *132,* 154104.

[49] Mahlberg, D.; Sakong, S.; Forster-Tonigold, K.; Groß, A. *J. Chem. Theory Comput.* **2019,** *15,* 3250-3259.

[50] Forster-Tonigold, K.; Groß, A. *J. Chem. Phys.* **2014,** *141,* 064501.

[51] Blöchl, P. E. *Phys. Rev. B* **1994,** *50,* 17953–17979.

[52] Allen, M. P.; Tildesley, D. J. *Computer Simulation of Liquids;* Oxford University Press: , 2017.

[53] Domínguez-Flores, F.; Groß, A.; Schmickler, W. *J. Phys. Chem. C* **2025,** *129,* 9179-9188.